Implications of the Super-K atmospheric, long baseline, and reactor data for the mixing angles θ_{13} and θ_{23}

J. Escamilla-Roa,[1] D. C. Latimer,[2] and D. J. Ernst[1]
[1]*Department of Physics and Astronomy, Vanderbilt University, Nashville, Tennessee 37235 USA*
[2]*Department of Physics and Astronomy, University of Kentucky, Lexington, Kentucky 40506 USA*
(Received 24 April 2009; published 8 January 2010)

A three-neutrino analysis of oscillation data is performed using the recent, more finely binned Super-K oscillation data, together with the CHOOZ, K2K, and MINOS data. The solar parameters Δ_{21} and θ_{12} are fixed from a recent analysis and Δ_{32}, θ_{13}, and θ_{23} are varied. We utilize the full three-neutrino oscillation probability and an exact treatment of Earth's Mikheyev-Smirnov-Wolfenstein (MSW) effect with a castle-wall density. By including terms linear in θ_{13} and $\varepsilon := \theta_{23} - \pi/4$, we find asymmetric errors for these parameters $\theta_{13} = -0.07^{+0.18}_{-0.11}$ and $\varepsilon = 0.03^{+0.09}_{-0.15}$. For θ_{13}, we see that the lower bound is primarily set by the CHOOZ experiment while the upper bound is determined by the low energy e-like events in the Super-K atmospheric data. We find that the parameters θ_{13} and ε are correlated—the preferred negative value of θ_{13} permits the preferred value of θ_{23} to be in the second octant, and the true value of θ_{13} affects the allowed region for θ_{23}.

DOI: 10.1103/PhysRevC.81.015501 PACS number(s): 14.60.Pq

I. INTRODUCTION

The experimental observation of neutrino oscillations implies that at least two of the three neutrinos have mass and the mass eigenstates differ from the flavor eigenstates. The vast majority of oscillation experiments [1–20], including the null result from the CHOOZ reactor experiment [21], can be globally understood in terms of three mixing angles θ_{jk} with $j = 1, 2, 3$ and $j < k$; one phase δ; and two independent mass-squared differences $\Delta_{kj} := m_k^2 - m_j^2$. The separation between two of the mass-squared differences is sufficiently large so that the data from a given experiment, which may span some range of baselines and neutrino energies, can be approximately understood within the context of an effective two-flavor theory. Experiments detecting solar neutrinos [1–10] and the long baseline (LBL) reactor experiment KamLAND [11,12] are particularly sensitive to the mixing angle θ_{12} and the mass-squared difference Δ_{21} assuming the standard representation of the neutrino mixing matrix [22,23]. A three-neutrino analysis [24] gives a value for the mixing angle $\sin^2\theta_{12} = 0.304^{+0.046}_{-0.034}$ ($2\ \sigma$ error), with a precision of 8% at 3σ. The solar mass-squared difference is determined predominantly by the KamLAND data [12] and is found to be $\Delta_{21} = 7.65^{+0.47}_{-0.40} \times 10^{-5}$ eV^2. Atmospheric and accelerator beam-stop neutrinos provide experimentalists with a good source with which to measure θ_{23} and Δ_{32}. MINOS [19,20] predominantly determines Δ_{32} while the mixing angle θ_{23} is determined mainly by the Super-K atmospheric data [13–16]. Present values for these parameters [24] are $\Delta_{32} = 2.40^{+0.24}_{-0.22} \times 10^{-3}$ eV^2 and $\sin^2\theta_{23} = 0.50^{+0.13}_{-0.11}$. The remaining mixing angle θ_{13} mixes the two scales. This same analysis gives $\sin^2\theta_{13} \leqslant 0.040$; recent analyses hint at a value of θ_{13} differing from zero [25–29]. Recent review articles can be found at Refs. [30,31].

As we enter the era of precision measurements, global analyses of neutrino data must employ a full three-neutrino framework to correctly assess the neutrino mixing parameters. This will become evident herein as we consider various experiments' impact upon the small parameters θ_{13} and $\varepsilon := \theta_{23} - \pi/4$, the deviation of θ_{23} from maximal mixing. The quantitative knowledge of θ_{13} is a particularly important part of neutrino oscillation phenomenology because it sets the magnitude of possible CP-violating effects as well as the size of effects that might be used to determine the neutrino mass hierarchy. There are presently three new reactor experiments planned or under construction which are designed to measure θ_{13}: Daya Bay [32], Double CHOOZ [33], and RENO [34]; an LBL experiment has just started running, T2K [35]. The subsequent generation of experiments, which will be designed to ascertain the level of CP violation, cannot proceed until the current generation better determines the value of θ_{13}. In addition, a more quantitative knowledge of the mixing angles, and particularly of θ_{13}, can help discern between models and symmetries of the physics that underlies neutrino mixing. If $\theta_{13} = 0$, then the data are consistent with tribimaximal mixing [36,37]; however, if this mixing angle differs appreciably from zero then other models [38–41] will need to be considered. The mixing matrix can then signify an underlying symmetry that may lead to an understanding of the origin of neutrino mass [42,43]. The deviation of θ_{23} from maximal mixing is also important in model building as it might indicate the presence of a broken symmetry. At short baselines, the oscillation probabilities that might probe the mixing angle θ_{13} are quadratic in this small parameter; however, we previously showed that there are terms in the oscillation probability linear in θ_{13} that are appreciable at very long baselines (VLBL) [44–48] and arise from interference between the oscillations driven by the two mass-squared differences. This is also a region of the parameter space where one can look [45,49] for CP-violating effects. The sub-GeV data set of the Super-K atmospheric experiments is potentially sensitive to such effects. Furthermore, it was shown in Ref. [48] that there is a nontrivial relation between ε and θ_{13} for sub-GeV neutrinos at VLBL's. As such, the extraction

of these parameters from the atmospheric data requires a full three neutrino treatment since approximations overly simplify the correlations among the parameters. A number of possible future experiments have been proposed so that the value of θ_{13}, the octant of θ_{23} (i.e., the value of ε), the size of the CP-violating phase δ, and the mass hierarchy question can be disentangled. How to do this with future atmospheric neutrino detectors can be found in Refs. [50–57].

We here investigate atmospheric neutrino oscillations with the full three-neutrino oscillation probabilities. Since we do not use truncated expansions, all terms linear in θ_{13} and ε will be considered as well as higher order contributions. We do not expect a large change in the extracted parameters as only a limited number of the Super-K data bins lie in the region where linear terms will be significant. On the other hand, in the context of atmospheric data, θ_{13} is itself a small effect as is the octant of θ_{23}. Small effects can sometimes have a proportionally larger impact on something that is inherently small. In keeping with the use of the full three-neutrino oscillation probabilities, we also utilize the method proposed in Refs. [58,59] to treat the Mikheyev-Smirnov-Wolfenstein (MSW) effect [60,61] with a castle-wall density profile of Earth. This treatment of the MSW effect is exact so that approximate expressions for the oscillation probabilities are not needed. This also means that the effects of parametric resonances are fully included.

II. ANALYSIS

In vacuo, the probability that a neutrino of flavor α and energy E_ν will be detected as a neutrino of flavor β after traveling a distance L is given by

$$\mathcal{P}_{\alpha\beta}(L/E_\nu) = \delta_{\alpha\beta} - 4\sum_{\substack{k<j,\\ j,k=1}}^{3}(U_{\alpha j}U_{\alpha k}U_{\beta k}U_{\beta j})\sin^2\varphi_{jk}, \qquad (1)$$

with $\varphi_{jk} := 1.27\,\Delta_{jk}\,L/E_\nu$, where L is measured in kilometers, E_ν in GeV, and the mass eigenvalues m_i in eV. The matrix $U_{\alpha i}$ is the unitary matrix that relates the mass basis i to the flavor basis α. We assume CP conservation so that the $U_{\alpha i}$ are real. Neutrinos that propagate long distances through matter of sufficient densities can incur significant interactions that are diagonal in flavor. For matters of constant density, the upshot of these interactions is a modification of the effective mixing angles and mass-squared differences so that an oscillation formula similar to Eq. (1) holds. The density of Earth may be approximated as a piecewise constant [62]. In addition, for certain energies and densities, the neutrinos can undergo parametric resonances [63–73] in regions of varying densities. To account for these interactions, we employ a simple model of Earth: a mantle of density 4.5 gm/cm^3 and a core of density 11.5 gm/cm^3 with a radius of 3486 km. Using the methods in Refs. [58,59], we are able to fully incorporate an exact three-neutrino model of the neutrino-matter interactions such that parametric resonances are automatically included.

Our interest is to study and extract the following parameters from the experimental data: θ_{13}, θ_{23}, and Δ_{32}. As such, we fix the solar mixing parameters from a recent analysis [30], $\theta_{12} = 0.58$ and $\Delta_{21} = 8.0\times10^{-5}$ eV^2. We use these parameters, which differ a small amount from those in Ref. [24], to be consistent with our earlier work [29]. Since the solar mass scale and atmospheric mass scale analyses are nearly independent, we find that the small differences in the choice of these parameters affects the results presented here at a level that is less than a line width on our curves. Given that there is no evidence to indicate CP violation, we assume CP conservation. In the standard parameterization of the neutrino mixing matrix, CP is conserved whenever the Dirac phase takes the values $\delta = 0, \pi$; alternatively, this convention is equivalent to setting $\delta = 0$ and allowing negative values for the mixing angle θ_{13}. We choose the latter bounds on these parameters as it produces a connected parameter space. We include the details of our analyses of the relevant experiments in the Appendix. We comment on them briefly here. The Super-K atmospheric data are statistically the most significant data set, and it covers a range of over 4 orders of magnitude in L/E. Our analysis employs the most recent, more finely binned data [16], a necessity for studying the small parameters θ_{13} and ε. We also include a model of the multiring events in the Super-K experiment, a subset that is often neglected. In addition, we include the most recent MINOS results [20], the K2K results [18], and the CHOOZ results [21].

To ascertain the importance of the linear and higher order terms in θ_{13} (and also ε), we compare our results with those generated by the often used subdominant approximation, which arises from an expansion in the ratio of the mass-squared differences, $\alpha \equiv \Delta_{12}/\Delta_{32}$. In this approximation, the leading order oscillation probabilities are given by

$$\begin{aligned}
\mathcal{P}_{ee} &= 1 - \sin^2 2\theta_{13}\,\sin^2(\varphi_{32}),\\
\mathcal{P}_{e\mu} &= \sin^2\theta_{23}\,\sin^2 2\theta_{13}\,\sin^2(\varphi_{32}),\\
\mathcal{P}_{\mu\mu} &= 1 - 4\cos^2\theta_{13}\,\sin^2\theta_{23}\,(1-\cos^2\theta_{13}\,\sin^2\theta_{23})\sin^2(\varphi_{32}).
\end{aligned} \qquad (2)$$

Additional correction terms [30,31,74] can then be added. The results for the subdominant approximation when compared to the results for the full three-neutrino oscillation probabilities will inform us of the size of the correction terms.

We begin by examining the mass-squared difference Δ_{32}. We plot $\Delta\chi^2$ versus Δ_{32} using both the subdominant approximation, Fig. 1(a), and the full three-neutrino calculation, Fig. 1(b), with θ_{13} and θ_{23} as varied parameters. The (black) solid curves are obtained from the Super-K atmospheric data alone. The (red) dash-dot curves employ the K2K, MINOS, and CHOOZ data, omitting the Super-K atmospheric data. These curves are largely determined by the recent MINOS data, which constrain the mass-squared difference more so than Super-K, as is well known. The analysis utilizing all of the data sets (atmospheric, K2K, MINOS, and CHOOZ) is depicted by the (blue) dashed curves. Notice that, although the Super-K atmospheric data are not as constraining as MINOS, it combines with MINOS to produce a reduced bound, particularly from above. In comparing the approximation, Fig. 1(a), with the full calculation, Fig. 1(b), we see that the subdominant approximation is useful for determining the mass-squared difference Δ_{32}. A very careful inspection will

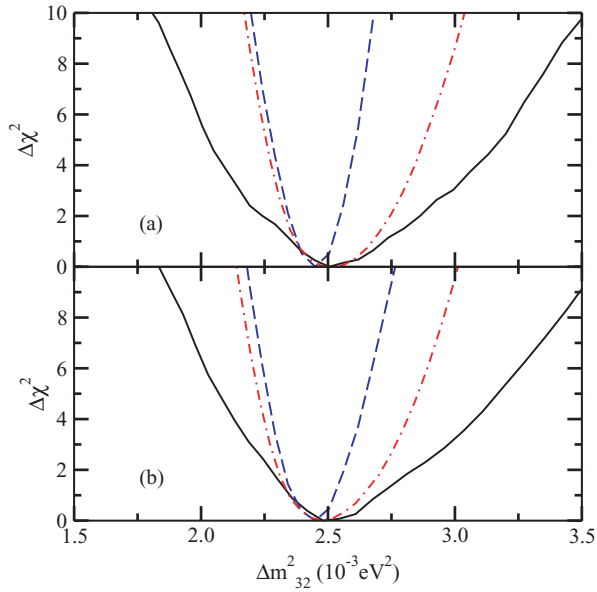

FIG. 1. (Color online) $\Delta\chi^2$ versus mass-squared difference Δ_{32} for the (a) subdominant approximation and (b) full three-neutrino calculation. The (black) solid curves utilize only atmospheric data; the (red) dot-dash curves utilize K2K, MINOS, and CHOOZ data; the (blue) dashed curves utilize all the data sets: atmospheric, K2K, MINOS, and CHOOZ.

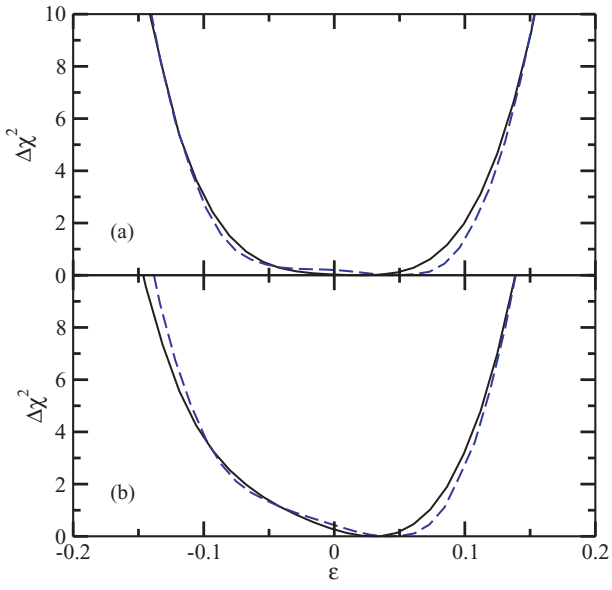

FIG. 2. (Color online) $\Delta\chi^2$ versus ε for the (a) subdominant approximation and (b) full three-neutrino calculation. The (black) solid curve utilizes only atmospheric data; the (blue) dashed curve utilizes all the data sets: atmospheric, K2K, MINOS, and CHOOZ.

reveal that the full three-neutrino analysis produces a slightly larger bound than does the subdominant approximation. Our results are $\Delta_{32} = 2.45^{+0.20}_{-0.15} \times 10^{-3}$ eV^2 at the 90% confidence level. (The errors quoted for our calculations will be for $\Delta\chi^2 = 6.25$, the 90% confidence level for a three-parameter fit.)

We next present $\Delta\chi^2$ versus $\varepsilon = \theta_{23} - \pi/4$ using the subdominant approximation, Fig. 2(a), and the full three-neutrino calculation, Fig. 2(b), with θ_{13} and Δ_{32} as varied parameters. We express our result in terms of θ_{23} rather than $\sin^2 2\theta_{23}$ or $\sin^2\theta_{23}$ because the oscillation probabilities truly are a function of θ_{23}. The (black) solid curve again represents the Super-K atmospheric data alone. The (blue) dashed curve represents the results from all data sets: Super-K atmospheric, K2K, MINOS, and CHOOZ. Adding K2K, MINOS, and CHOOZ hardly alters the Super-K result. We do not present the results for K2K, MINOS, and CHOOZ alone because these data do not yield a reasonable constraint on θ_{23} when treated as a linear variable with a varied θ_{13} included in the analysis. Only in a two-neutrino analysis do K2K and MINOS restrict the then appropriate variable $\sin^2 2\theta_{23}$. Comparing the subdominant approximation with the full calculation, we see that the full three-neutrino probabilities produce an allowed region, which is much more asymmetric about $\varepsilon = 0$. In fact, we find a statistically insignificant indication that θ_{23} is greater than $\pi/4$, maximal mixing. The ability of atmospheric data to determine the octant of θ_{23} was also investigated in Ref. [75]. We find the value at 90% CL is $\varepsilon = 0.03^{+0.09}_{-0.15}$.

In Fig. 3(a), we present $\Delta\chi^2$ versus θ_{13} calculated in the subdominant approximation and full three-neutrino formulation with θ_{23} and Δ_{32} as varied parameters. Previously, it was shown [16] that in the subdominant approximation the atmospheric data alone restrict θ_{13}. Focusing upon our subdominant calculation, Fig. 3(a), the (black) solid curve depicts the corresponding result from our analysis. As noted in the Appendix, our analysis quantitatively reproduces the results in Ref. [16]; for $\Delta\chi^2 < 4.6$, we both find $\sin^2\theta_{13} < 0.14$ (or $|\theta_{13}| < 0.38$). This is a very important calibration of our analysis tool. The effect of θ_{13} on atmospheric oscillations is small and obtaining the same result implies we are reproducing

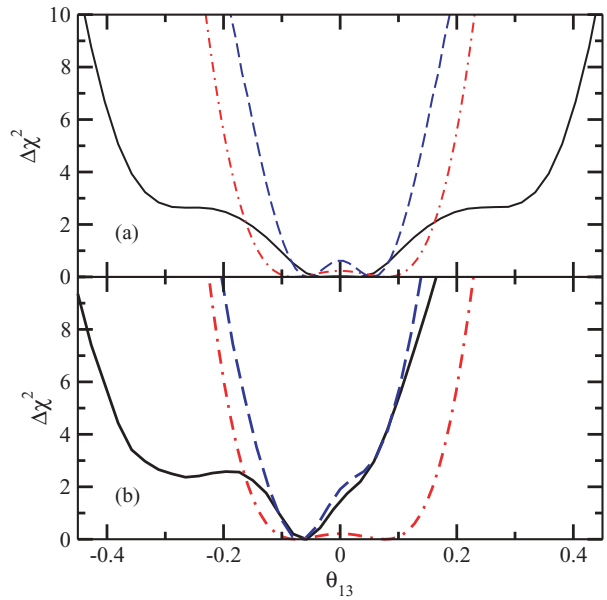

FIG. 3. (Color online) The same as Fig. 1 except $\Delta\chi^2$ versus θ_{13} is presented.

small effects, not just the global features of the analysis. The (red) dash-dot curve in Fig. 3(a) is the result of analyzing the K2K, MINOS, and CHOOZ data, neglecting the Super-K atmospheric data. This curve is mainly determined by the CHOOZ data. We see that CHOOZ data are more constraining on θ_{13} than are the Super-K atmospheric data. However, the (blue) dashed curve presents the results utilizing all of the data sets and shows that the Super-K data do somewhat reduce the error on θ_{13}; this is due to the indirect effect arising from Super-K further constraining the mass-squared difference Δ_{23}. To obtain the constraints on θ_{13} implied by the Super-K atmospheric data, it is important to use the data from Ref. [16], which are more finely binned than earlier Super-K work [15]. Note that the curves in the subdominant approximation are symmetric about $\theta_{13} = 0$ as is manifest from the approximate oscillation formulas, Eq. (2). In Refs. [25,26,28], it was observed that recent data imply a statistically insignificant nonzero value for θ_{13}; our results are likewise consistent.

Turning to the full three-neutrino calculation, Fig. 3(b), we find $\Delta\chi^2$ to be very asymmetric with a strong preference for negative θ_{13} when using only Super-K data, the (black) solid curve. The (red) dash-dot curve employs only K2K, MINOS, and CHOOZ data; it is symmetric about the origin so that the asymmetry present when all data are included, the (blue) dashed curve is due to the Super-K data. What is more, we see the novel result [29] that θ_{13} is constrained from above by the Super-K atmospheric data not by CHOOZ, while it is constrained from below primarily by CHOOZ.

This conclusion is further reinforced by looking at the allowed region for the parameters θ_{13} and θ_{23} as depicted in Fig. 4. We plot the $\Delta\chi^2 = 4.61$ contour, minimizing with respect to the third parameter Δ_{32} in calculating these curves. The (green) dash-dot curve depicts the results for Super-K atmospheric data alone in the subdominant approximation. We compare this with the (red) dashed curve, which also utilizes only the Super-K atmospheric data alone, but incorporates the full three-neutrino probabilities. Again, we see the significant change brought about by incorporating the linear and higher order terms in θ_{13}. The allowed region grows, favoring negative θ_{13}. The (blue) dash-dot-dot curve utilizes all the data in the subdominant approximation. It is similar to the (green) dash-dot curve because the mass-squared difference Δ_{32} is fixed when calculating the curves; the main effect of the MINOS experiment is to restrict Δ_{32}. Finally, the (black) solid curve utilizes all the data and the full three-neutrino oscillation probabilities. Note that the upper bound on θ_{13} is similar to that from the (red) dashed curve, that is, the curve also utilizing the full three-neutrino oscillation probabilities with only the Super-K data. For the lower bound on θ_{13}, however, we find similarities to the (blue) dash-dot-dot curve where the restriction on θ_{13} originates primarily from the CHOOZ experiment. Thus, we again see that the upper bound on θ_{13} no longer arises from the CHOOZ experiment, but is determined by the Super-K atmospheric experiment, while the lower bound continues to come from the CHOOZ experiment. Our final result for this mixing angle is $\theta_{13} = -0.07^{+0.18}_{-0.11}$. (As before, the errors quoted for our calculations are for $\Delta\chi^2 = 6.25$, the 90% confidence level for a three-parameter fit.)

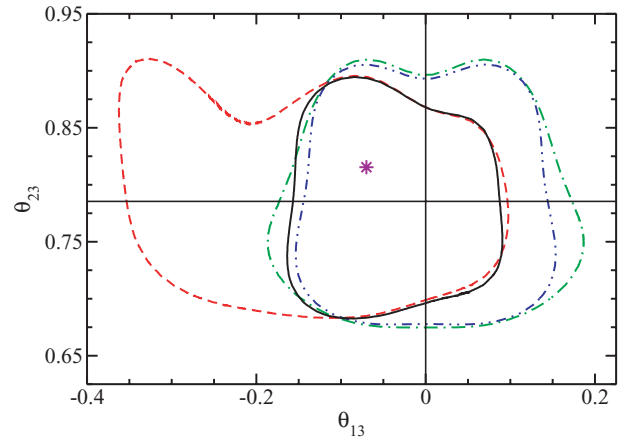

FIG. 4. (Color online) The $\Delta\chi^2 = 4.61$ contours for the parameters θ_{13} and θ_{23}. The (black) solid curve uses the full three-neutrino oscillation probabilities and all the data sets: CHOOZ, K2K, MINOS, and Super-K atmospheric. The (blue) dash-dot-dot curve represents the use of the subdominant approximation and all the data sets. The (red) dashed curve depicts the use of the full three-neutrino oscillation probabilities and only the Super-K data. The (green) dash-dot curve depicts the use of the subdominant approximation and the Super-K data alone. The vertical (horizontal) straight line marks $\theta_{13} = 0.0$ ($\theta_{23} = \pi/4$). The (violet) star indicates the location of the minimum for the analysis that includes all the data sets and the use of the full three-neutrino oscillation probabilities.

The principle effect of utilizing the full three-neutrino oscillation probabilities is the alteration of the shape of the allowed region for θ_{13}, particularly the introduction of the asymmetry about zero. The absolute minimum for χ^2 is lowered by only 1.3 [29]. This is because the minima are very close to $\theta_{13} = 0$, where the linear and higher order terms contribute little.

III. DISCUSSION

The most striking differences between the subdominant approximation and the full three-neutrino probabilities are seen in the determination of the mixing angle θ_{13} in Fig. 3. Additionally, the deviation of θ_{23} from maximal mixing also produces noticeable features, though less striking in Fig. 2. Clearly, the two features are nontrivially linked, as demonstrated in the allowed regions depicted in Fig. 4. In fact, we see from Fig. 3 that the Super-K data are the source of the asymmetry about $\theta_{13} = 0$ in the full three-neutrino model. To flesh out which subset of the Super-K data results in these asymmetries, we examine the various contributions of the data to χ^2 for a fixed positive and negative value of the mixing angle θ_{13} taken to be ± 0.15. The total difference in $\Delta\chi^2$ for $\theta_{13} = +0.15$ and $\theta_{13} = -0.15$ is ~ 7.0. Focusing on the fully contained events, we find that two-thirds of this change in $\Delta\chi^2$ between the positive and negative values of the mixing angle comes from the sub-GeV electron-like events. Half of the total change in $\Delta\chi^2$ (3.5) arises from a single angular bin within this subset of data, namely the bin for e-like events in which the detected charged lepton has zenith angle ϑ satisfying $-0.8 < \cos\vartheta < -0.6$ and momentum less than

250 MeV/c. The detected leptons in this bin are produced by neutrinos that travel along a VLBL upward through the Earth. Such neutrinos fall into the region of L/E where effects linear in θ_{13} are significant in the oscillation probabilities $\mathcal{P}_{e\mu}$ and $\mathcal{P}_{\mu\mu}$ [44–48]; such effects occur in a region where the subdominant approximation is the leading term in an expansion that is not convergent. For VLBL's, the oscillation phase $\varphi_{21} = 1.27\,\Delta_{21}\,L/E_\nu$ due to the solar mass-squared difference Δ_{21} is near $\pi/2$. In this case, one cannot treat α, the ratio of the mass-squared differences, as a small correction. Analytic expressions for the oscillation probabilities valid in this region can be found in Ref. [76]. Terms linear in θ_{13} can be even more significant [77] should an atmospheric oscillation experiment be able to take data at energies below 100 MeV. We comment that the angular bin $-1.0 < \cos\vartheta < -0.8$ is also in this L/E region for the low-energy neutrinos; however, a typical neutrino that produces leptons in this bin passes through Earth's higher density core. We find that the core suppresses the oscillations, and thus this angular bin is not as sensitive to the effects linear in θ_{13}.

The preference of the data for negative θ_{13} can be linked to the excess of e-like events in the sub-GeV data set [45]. This excess is not present in the μ-like data or in the multi-GeV data so that an overall renormalization of the atmospheric flux cannot account for the excess. To understand the role of the data in extracting θ_{13} and θ_{23}, we examine the relevant oscillation probabilities in the limit of a constant density mantle and sub-GeV neutrino energies, keeping only terms linear in θ_{13} and ε and averaging over the Δ_{32} oscillations; these approximations were discussed previously [45,48]. As detailed in the Appendix, the electron-like events at the Super-K detector are related to the ν_e survival probability and the ν_μ conversion probability via $\mathcal{R}_e = \mathcal{P}_{ee} + r\mathcal{P}_{e\mu}$, where r is the ratio of the ν_μ to ν_e flux at the source. This yields the approximate expression

$$\mathcal{R}_e \approx 1 + r\sin^2 2\theta_{12}^m \left[\frac{1}{2} - \frac{1}{r} + \cot\left(2\theta_{12}^m\right)\theta_{13} - \varepsilon\right]\sin^2\varphi_{21}^m. \tag{3}$$

Here, θ_{12}^m is the effective mixing angle in matter; additionally, the phase φ_{21}^m employs the effective mass-squared difference in matter corresponding to Δ_{21}. In this approximation, we can understand how to effect an excess of electron-like events for sub-GeV neutrinos over a LBL,

$$\frac{1}{2} - \frac{1}{r} + \cot\left(2\theta_{12}^m\right)\theta_{13} - \varepsilon > 0. \tag{4}$$

Using the same approximations, we can simply express the MSW resonant energy

$$E_R = \frac{\Delta_{21}\cos 2\theta_{12}}{2V\cos^2\theta_{13}}, \tag{5}$$

with $V \approx 1.7 \times 10^{-13}$ eV in the mantle; this yields E_R on the order of 100 MeV. This resonance is apparent when we plot the eigenvalues of the effective mass-squared matrix in the mantle, Fig. 5; the "resonance" is indicated by the slight bowing in the curves toward each other and is located at the point where the effective mass-squared difference is minimal.

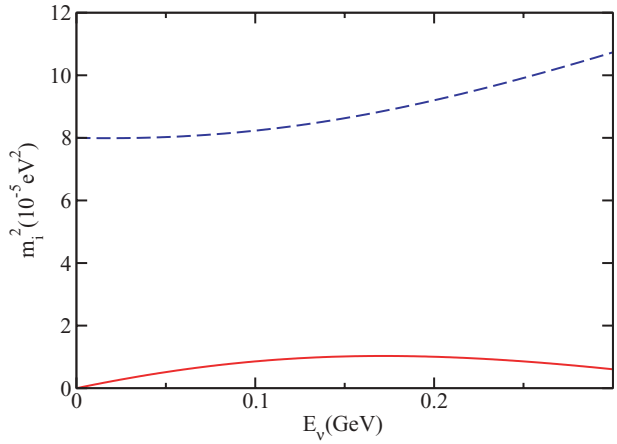

FIG. 5. (Color online) The two lowest eigenvalues of the effective mass matrix in a constant density mantle as a function of neutrino energy E_ν. The (red) solid curve is $(m_1)^2(E_\nu)$, and the (blue) dashed curve is $(m_2)^2(E_\nu)$.

At the resonant energy, one has $\theta_{12}^m = \pi/4$; for neutrino energies above the resonance, the effective mixing angle in matter increases up to $\pi/2$. As a consequence, for neutrino energies above 100 MeV in the mantle, the function $\cot(2\theta_{12}^m)$ is negative; to reiterate, the coefficient of the θ_{13} term in the inequality found in Eq. (4), is negative. We note that for these low-energy atmospheric neutrinos $r \sim 2$ so that the first two terms of the inequality approximately sum to zero. If θ_{13} is restricted to positive values, then the mixing angle θ_{23} must lie in the first octant ($\varepsilon < 0$) to account for the excess in $\mathcal{R}_e$. However, if we allow θ_{13} to run the full range of allowed parameter space in a CP-conserving theory, then a negative value of this mixing angle can easily accommodate the excess in $\mathcal{R}_e$, even permitting θ_{23} to lie in the second octant, as is the case in our analysis.

To demonstrate the point regarding the effect of terms linear in θ_{13}, we plot $\mathcal{R}_e$ in Fig. 6 for sub-GeV neutrinos in angular

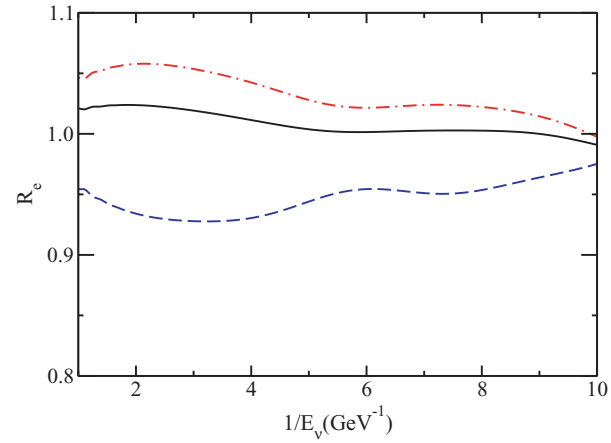

FIG. 6. (Color online) The experimentally measured quantity $\mathcal{R}_e$ versus the inverse neutrino energy E_ν^{-1} in the sub-GeV region for angular bin $-0.8 < \cos\vartheta < -0.6$. The (black) solid curve is the result for the best fit parameters, the (red) dash-dot curve is for $\theta_{13} = -0.15$, and the (blue) dashed curve is the result for $\theta_{13} = +0.15$.

bin $-0.8 < \cos\vartheta < -0.6$. The (black) solid curve employs our best fit parameters. To show the effect of θ_{13}, we also plot the e-like events for $\theta_{13} = \pm 0.15$ with Δ_{23} and θ_{23} unchanged. The (red) dash-dot curve has negative θ_{13}, and the (blue) dashed curve has positive θ_{13}. It is clear that a negative value of this mixing angle permits an excess of e-like events for sub-GeV neutrinos.

Returning to Fig. 4, we see how the full three-neutrino oscillation probabilities jointly affect the allowed region for the two mixing angles θ_{23} and θ_{13}. Using the subdominant approximation, the (blue) dash-dot-dot curve represents the allowed region when all the data are employed. As expected, the region is symmetric about $\theta_{13} = 0$, and we note that the actual value of θ_{13} has little impact upon the allowed values of θ_{23}, save the neighborhood immediately around $\theta_{13} = 0$. Inclusion of the higher order terms in the oscillation probability dramatically alters this picture. As discussed previously, the data now favor negative θ_{13}, with the atmospheric Super-K data shrinking the contour, the (black) solid curve, for positive θ_{13}. No longer is the contour symmetric about a particular value of θ_{13}; hence, the true value of this mixing angle will impact the allowed region for the θ_{23} mixing angle. In particular, the allowed region for θ_{23} shrinks as θ_{13} approaches positive values. In the future, should a reactor neutrino experiment confirm a nonzero value for $|\theta_{13}|$, it will have interesting consequences for the allowed value of θ_{23}. With such a measurement, we will perhaps see two true local minima in the $\Delta\chi^2$ versus θ_{13} plot in Fig. 3. The impact upon Fig. 4 will be to separate the jointly allowed regions into two disconnected curves with the limit on θ_{23} more tightly constrained for positive values of θ_{13}.

IV. CONCLUSIONS

As we enter into the era of precision neutrino experiments, small effects, such as those arising from θ_{13} or the octant of θ_{23}, require a careful treatment in the analysis. Future reactor experiments [32–34] are sensitive to θ_{13}^2 and thus can determine the magnitude of θ_{13}, but not its sign. LBL experiments, for example, [35], will contain small effects that are linear in θ_{13}, while an upgraded Super-K will produce additional data in the region where we find significant effects linear in θ_{13}. How these different data interplay with each other in determining θ_{13}, including its sign, and the octant of θ_{23} will be most interesting.

In Ref. [78], it was shown that the constancy of R_e imposes an upper bound on $|\theta_{13}|$ as well as constrains θ_{23} to be near maximal mixing. We find that present atmospheric data restrict the value of θ_{13} from above, while the limit from below remains as determined by CHOOZ. We find $\theta_{13} = -0.07^{+0.18}_{-0.11}$, assuming no CP violation. We investigate which data points lead to the asymmetry in θ_{13} and find that it is the atmospheric data in the VLBL region previously noted [44–48] to have significant terms linear in θ_{13}. We further find that Earth's MSW effect plays an important role as it increases the effective value of θ_{12}^m in matter such that the atmospheric data provide a strict upper bound on θ_{13}. Further, the data producing the preference for a negative θ_{13} are data with an excess of e-like events, $\mathcal{R}_e > 1$. Allowing θ_{13} to be negative supports this excess and permits θ_{23} to be in the second octant. The parameters θ_{13} and θ_{23} are found to be correlated; the statistically insignificant negative value for the minimum of θ_{13} relates to the minimum for θ_{23} being statistically insignificantly in the second octant, and the error in θ_{23} is dependent on the value of θ_{13}. Future measurements of θ_{13} will impact the allowed value for θ_{23}.

For Δ_{32} and θ_{23} we find $\Delta_{32} = 2.45^{+0.20}_{-0.15} \times 10^{-3}$ eV^2 and $\theta_{23} - \pi/4 = 0.03^{+0.09}_{-0.15}$, where the use of the full three-neutrino oscillation probabilities leads to the asymmetry in the errors. We find that a quantitative analysis requires utilizing the more finely binned atmospheric data of Ref. [16], the use of the full three-neutrino oscillation probabilities, and the inclusion of the full three-neutrino MSW effect.

ACKNOWLEDGMENTS

The work of J.E-R. and D.J.E. is supported, in part, by US Department of Energy Grant No. DE-FG02-96ER40975. The work of J.E-R. is also supported, in part, by CONACyT, Mexico. The work of D.C.L. is supported, in part, by US Department of Energy Grant No. DE-FG02-96ER40989.

APPENDIX A: EXPERIMENTAL SIMULATION

In this appendix, we present the computational tools we use to analyze the Super-K atmospheric, CHOOZ, K2K, and MINOS experiments. The analysis tool for the Super-K atmospheric data is similar to that being used by others [24,30,31]; however, it is distinct in that we employ a full three-neutrino oscillation probability rather than an approximate expansion, use a full three-neutrino treatment of Earth's MSW effect, and include a model of the multiring data. The analysis of CHOOZ, K2K, and MINOS data is standard. Additional details can be found in Ref. [79]. Also, in this appendix, we demonstrate the efficacy of our analysis tools by comparing our results with others when appropriate.

The Appendix is organized as follows. We first discuss the Super-K atmospheric experiment, beginning with the contained events followed by the upgoing muon events. Then we discuss our statistical treatment of this experiment. Finally, we include a similar discussion for the CHOOZ, K2K, and MINOS experiments.

1. Super-K contained events

To observe atmospheric neutrinos at Super-K, the neutrinos must interact with matter in either the detector or the surrounding environ to produce charged particles. The direction and energy of these charged particles can be deduced from the Cherenkov light they emit while traveling through the water-filled detector; from this data one can infer, on average, the direction and energy of the initial neutrino. The Super-K experiment classifies the various detections in terms of the production point of the charged lepton, the number of charged particles produced, and their subsequent motion through the detector.

Contained events refer to events in which the charged lepton is produced by the neutrino within the detector. These events are subdivided into fully contained and partially contained events. If an event is fully contained, then the charged lepton(s) produced within the detector do not escape the detector. An event is partially contained if the charged lepton(s) exits the detector. Finally, these two data sets are further separated into single-ring and multiring events according to the number of charged particles produced by the neutrino; if only one charged lepton is observed in the detector, it is termed a single-ring event. We first discuss the fully contained single-ring events and then extend this analysis to the other classes of data. The fully contained single-ring events are statistically the most significant subset of the data and the cleanest to analyze. Preliminary discussions of the analysis technique utilized for the fully contained events can be found in Refs. [80,81].

The Super-K detector distinguishes between electrons and muons by the fuzziness of the Cherenkov ring generated by the charged lepton; however, the detector cannot differentiate an electron e^- from a positron e^+ or a μ^- from a μ^+. Given flavor and charge conservation, the detector can only determine if an event is e-like, originating from either a ν_e or $\overline{\nu}_e$ interaction, or μ-like, originating from either a ν_μ or $\overline{\nu}_\mu$ interaction. Thus, the detector counts charged leptons of flavor α in energy bin m and zenith angular bin n over the run time T

$$N_\alpha^{nm} = \sum_{\nu,\overline{\nu}} \left(\frac{\mathrm{d}N_{\alpha\to\alpha}^{nm}}{\mathrm{d}t} + \frac{\mathrm{d}N_{\beta\to\alpha}^{nm}}{\mathrm{d}t} \right) T, \tag{A1}$$

where the quantity $\mathrm{d}N_{\beta\to\alpha}^{nm}/\mathrm{d}t$ represents the rate at which a neutrino, created in the atmosphere with flavor β, will be detected as an α-like event in the appropriate energy and angular bins within the detector.

This rate depends upon the atmospheric neutrino flux, the neutrino oscillation probability from source to detector, the kinematics of the charged lepton production, and the detector efficiencies. We may write it as

$$\begin{aligned} \frac{\mathrm{d}N_{\alpha\to\beta}^{nm}}{\mathrm{d}t} = N \int_{E_{\mathrm{vis}}^{m,\min}}^{E_{\mathrm{vis}}^{m,\max}} \mathrm{d}E_{\mathrm{vis}} \int \mathrm{d}\cos\theta_\nu \int \mathrm{d}E_\nu \int \mathrm{d}\cos\theta_s \int \mathrm{d}\phi_s \\ \times \varepsilon(E_{\mathrm{vis}}) \frac{\mathrm{d}^2\,\Phi_\alpha(E_\nu, \cos\theta_\nu)}{\mathrm{d}E_\nu\,\mathrm{d}\cos\theta_\nu} \tilde{\mathcal{P}}_{\alpha\beta}(E_\nu, \cos\theta_\nu) \\ \times \frac{\mathrm{d}^3\sigma_\beta(E_\nu;\ E_\ell,\ \cos\theta_s)}{\mathrm{d}E_\ell\,\mathrm{d}\cos\theta_s\,\mathrm{d}\phi_s} \\ \times \Theta(\cos\vartheta^{n,\max} - \cos\vartheta)\ \Theta(\cos\vartheta - \cos\vartheta^{n,\min}). \end{aligned} \tag{A2}$$

We define the variables in Eq. (A2). N represents the number of target protons. E_{vis} is the energy measured by the detector (this quantity is defined differently depending on the data sample); $E_{\mathrm{vis}}^{m,\max}$ ($E_{\mathrm{vis}}^{m,\min}$) is the maximum (minimum) value of E_{vis} for bin m. (For single-ring fully contained events, E_{vis} is simply the energy of the created lepton, $E_{\mathrm{vis}} = E_\ell$.) ϑ is the zenith angle of the detected charged lepton with $\cos\vartheta = 1$ indicating the vertically downward direction. The relative angle between the incident neutrino and the produced charged lepton are described by the θ_s scattering angle and the ϕ_s azimuthal angle. The energy of the incident neutrino is E_ν with zenith angle θ_ν. The azimuthally averaged atmospheric neutrino flux for a neutrino of flavor α is $\mathrm{d}^2\,\Phi_\alpha(E_\nu, \cos\theta_\nu)/\mathrm{d}E_\nu\,\mathrm{d}\cos\theta_\nu$, which we take from Ref. [82]. $\varepsilon(E_{\mathrm{vis}})$ corresponds to the detection efficiency. $\mathrm{d}^3\sigma_\beta(E_\nu;\ E_\ell,\ \cos\theta_s)/\mathrm{d}E_\ell\,\mathrm{d}\cos\theta_s\,\mathrm{d}\phi_s$ is the differential cross section for a neutrino of energy E_ν and flavor β to produce a charged lepton of flavor β with energy E_ℓ through a scattering angle θ_s. Although the differential cross section that occurs in Eq. (A2) does not depend on the azimuthal angle ϕ_s, the geometry that determines in which angular bin an event lies does depend on ϕ_s. This is because the zenith angle ϑ of the charged lepton is given in terms of the neutrino zenith angle θ_ν and the scattering angles θ_s and ϕ_s by

$$\cos\vartheta = \cos\theta_s\ \cos\theta_\nu - \sin\theta_s\ \sin\theta_\nu\ \cos\phi_s. \tag{A3}$$

The energy range for atmospheric neutrinos as measured at Super-K requires the use of several cross sections. At low energies, below 1 GeV, the dominant process is charged-current quasielastic scattering from the proton and the nucleons in the oxygen nucleus in H_2O, for example, $\overline{\nu}_e + p^+ \to e^+ + n$ and $\nu_e + n \to e^- + p^+$. At intermediate energies, peaking around 1.5 GeV, the dominant process is a single-pion resonance production, that is, $\nu_\alpha + N \to \ell_\alpha + N^*$ followed by $N^* \to N' + \pi$. At higher energies, starting at 1 GeV and dominating above 10 GeV, deeply inelastic scattering occurs, $\nu_\alpha + N \to \ell_\alpha + X$. We utilize the same set of cross sections as was used in Ref. [15]. The Heaviside functions are inserted into Eq. (A2) to restrict the values of θ_ν, θ_s, and ϕ_s to values that produce a value for ϑ that lies within bin n.

The incident neutrino's zenith angle θ_ν does not uniquely determine the path length L, as neutrinos are produced at a variety of vertical heights, h, in the atmosphere. We thus introduce the oscillation probability $\tilde{\mathcal{P}}_{\alpha\beta}(E_\nu, \cos\theta_\nu)$ averaged over this production height in the atmosphere

$$\tilde{\mathcal{P}}_{\alpha\beta}(E_\nu, \cos\theta_\nu) = \int_0^\infty \mathrm{d}h\ \mathrm{P}_\alpha(h,\ E_\nu)\, \mathcal{P}_{\alpha\beta}(L(h, \cos\theta_\nu)/E_\nu), \tag{A4}$$

where L is related to h and $\cos\theta_\nu$ by

$$L = \sqrt{R^2\ \cos^2\theta_\nu + h\,(2R + h)} - R\ \cos\theta_\nu, \tag{A5}$$

with R the radius of Earth. $\mathrm{P}_\alpha(h, E_\nu)$ is the normalized probability for a neutrino of flavor α to be created at a height h, a quantity we take from Ref. [83].

The neutrino oscillation probability in vacuum $\mathcal{P}_{\alpha\beta}(L/E_\nu)$ is given in Eq. (1); however, the coherent forward scattering of neutrinos on matter alters the probability for those neutrinos which pass through Earth [60,61]. Neutral current interactions between the neutrinos and matter are not flavor dependent, leaving the oscillation probabilities unaffected; however, charged current interactions will introduce into the Hamiltonian a flavor-dependent potential. In the flavor basis, we may write [84–86] the neutrino evolution equation as

$$i\,\partial_t \nu_f = \left(\frac{1}{2E_\nu} U \mathcal{M} U^\dagger + \mathcal{V} \right) \nu_f, \tag{A6}$$

where $\mathcal{M} = \mathrm{diag}\,(0, \Delta_{21}, \Delta_{31})$ and the operator $\mathcal{V}$ operates on only the electron flavor with a magnitude $\mathcal{V} = \sqrt{2} G_F N_e(x)$ in which $N_e(x)$ is the electron number density of the matter. We note that for antineutrinos, this potential has the opposite algebraic sign. In matter of constant density, one may diagonalize the Hamiltonian to determine the effective mass-squared differences in a new propagation basis; this basis is related to the flavor states by a modified effective mixing matrix in the matter. The density of the Earth may be approximated as a piecewise constant [62] so that neutrinos that travel through the Earth may traverse regions of varying density. For certain energies and mixing angles, neutrinos can undergo parametric resonances when passing through regions of different densities [63–73]. For a piecewise constant density profile, we may use the the methods of Refs. [58,59] to exactly determine the neutrino oscillation probability. This method is computationally efficient as it merely involves finding the local effective mass-squared differences and mixing angles, and its exactness accurately accounts for effects that depend on small parameters or effects due to parametric resonances.

The full calculation represented by Eq. (A2) is a numerically intensive five-dimensional integration. We desire an analysis tool that is both numerically accurate and sufficiently computationally efficient so that we can scan a large swath of parameter space in a reasonable amount of time. To effect this, we make approximations in Eq. (A2) regarding the scattering angle and efficiency terms. First, we fix the scattering angle θ_s to its average value $\overline{\theta}_s$ as a function of $E_{\mathrm{vis}} = E_\ell$ for each energy and angular bin as calculated by the Monte Carlo simulations in Ref. [87]. This eliminates the integral over $\cos\theta_s$. We are justified in doing so because, if this integral is done last, the integrand is quite smooth and nearly linear over each bin, particularly for the finer binning of the most recent data. Thus, we expect this approximation to be quantitatively accurate and this is what we find. With this approximation, Eq. (A2) becomes

$$\begin{aligned}\frac{\mathrm{d}N^{nm}_{\alpha\to\beta}}{\mathrm{d}t} = N \int_0^\infty \mathrm{d}E_\nu \int_{E^{m,\min}_{\mathrm{vis}}}^{E^{m,\max}_{\mathrm{vis}}} \mathrm{d}E_{\mathrm{vis}} \int \mathrm{d}\cos\theta_\nu \int \mathrm{d}\phi_s \\ \times \varepsilon(E_{\mathrm{vis}}) \frac{\mathrm{d}^2\,\Phi_\alpha(E_\nu, \cos\theta_\nu)}{\mathrm{d}E_\nu\,\mathrm{d}\cos\theta_\nu} \tilde{\mathcal{P}}_{\alpha\beta}(E_\nu, \cos\theta_\nu) \\ \times \frac{\mathrm{d}^2\sigma_\beta[E_\nu;\, E_\ell, \cos\overline{\theta}_s(E_{\mathrm{vis}})]}{\mathrm{d}E_\ell\,\mathrm{d}\phi_s} \\ \times \Theta(\cos\vartheta^{n,\max} - \cos\vartheta)\ \Theta(\cos\vartheta - \cos\vartheta^{n,\min}),\end{aligned} \tag{A7}$$

where the differential cross section and the angle ϑ are evaluated at $\cos(\theta_s) = \cos(\overline{\theta}_s)$.

Finally, we must determine the detector efficiency $\varepsilon(E_{\mathrm{vis}})$, which was not furnished by the experimentalists. We can, however, extract it from information provided. For no oscillations, Eq. (A2) becomes, utilizing our assumptions,

$$\begin{aligned}\frac{\mathrm{d}N^m_\alpha}{\mathrm{d}t} = \overline{\varepsilon}(m)\, N \int_0^\infty \mathrm{d}E_\nu \int_{E^{m,\min}_{\mathrm{vis}}}^{E^{m,\max}_{\mathrm{vis}}} \mathrm{d}E_{\mathrm{vis}} \int \mathrm{d}\cos\theta_\nu \int \mathrm{d}\phi_s \\ \times \frac{\mathrm{d}\,\Phi_\alpha(E_\nu, \cos\theta_\nu)}{\mathrm{d}E_\nu \mathrm{d}\cos\theta_\nu} \frac{\mathrm{d}^3\sigma_\beta[E_\nu;\, E_\ell, \cos\overline{\theta}_s(E_{\mathrm{vis}})]}{\mathrm{d}E_\ell\,\mathrm{d}\cos\theta_s\,\mathrm{d}\phi_s},\end{aligned} \tag{A8}$$

where we assume that the efficiency is primarily dependent on the lepton energy, $\varepsilon(E_{\mathrm{vis}})$. Further, taking it as a constant $\overline{\varepsilon}(m)$ over each energy bin m, we pull it out of the integral. The Monte Carlo calculation of $\mathrm{d}N^m_\alpha/\mathrm{d}t$ appears in Ref. [88]. Performing the integrals on the right-hand side of Eq. (A8), we can use the Monte Carlo result to determine the average efficiency $\overline{\varepsilon}(m)$ for each energy bin. This average is then used in Eq. (A7).

To conclude the discussion of the single-ring fully contained analysis, we note that there are ten angular bins of equal size in $\cos\vartheta$, going from $+1$ (downward) to -1 (upward); ten energy bins for e-like events; and eight energy bins for μ-like events. In total, this subset of the data consists of 180 data points.

Within the fully contained data set, we also have multiring events. These data correspond to neutrinos that interact inside the detector to produce more than one detected particle in the final state. We can calculate the multiring event rate in a manner similar to the single-ring event rate provided we modify the visible energy and neutrino event direction. In a multiring event, the visible energy depends on the number of particles in the final state, their momenta, and their scattering angles. There is no simple and reliable way of determining E_{vis}; as such, we must make an approximation. We use the results of Monte Carlo simulations given in Ref. [87] to estimate the average value of E_ν/E_{vis} for each energy bin.

To determine the angular distribution of these events, we follow the experimentalists and assign a single scattering angle to the final state particles. To model the angular distribution of the multiring sample, we define an average multiring scattering angle for all particles in energy bin m as $\overline{\theta}_{\mathrm{mr}}(m)$. To match with the no oscillation results of the experimentalists and include this average scattering angle, we adjust $\overline{\theta}_{\mathrm{mr}}(m)$ for each angular bin and each energy bin such that our no-oscillation calculation reproduces the corresponding experimentalists' Monte Carlo no-oscillation results [88]. The multiring calculation now has the same numerical structure as the single-ring calculation. This allows us to obtain the efficiencies just as we did for the single-ring events. Our analysis then uses Eqs. (A1), (A2), and (A3) to calculate the event rate for the multiring events. Given the limited information provided by the experimentalists, we believe that this approach, which buries many unknowns into matching the no-oscillation calculation with the experimentalists' Monte Carlo calculation and uses an effective E_{vis} taken from the experimentalists' Monte Carlo calculation, is as good as is possible. It does reproduce the results found in [87,88].

The next data set consists of the partially contained events. In these, the charged lepton is created within the detector, but has sufficient energy to escape the inner detector and be detected by the outer detector. If the energy deposited in the outer detector appears to be less than that needed for a muon to traverse the outer detector, the event is classified as an outer detector stopped event; those depositing more energy are termed outer detector through-going. We alter the definition of the visible energy

$$E_{\mathrm{vis}} = E_{\mathrm{inner}} + E_{\mathrm{dead}} + E_{\mathrm{anti}}, \tag{A9}$$

with $E_{\rm inner}$ the total energy of the charged particle observed in the inner detector, $E_{\rm dead}$ the energy deposited in the region between the inner detector and the outer detector, and $E_{\rm anti}$ the energy observed in the outer detector. The charged lepton energy is then a function of this visible energy; we set $E_\ell(E_{\rm vis})$ to its average value as taken from the Monte Carlo calculations from Ref. [87]. The efficiencies are similarly taken for each data bin from the same Monte Carlo no-oscillation calculations as described previously. For these single-ring partially contained events, the same ten angular bins are used and there are four energy bins each for both the outer detector stopped and through-going events, giving a total of 80 data points.

2. Upgoing muons

A second major subset of the atmospheric data arises from detecting muons created by atmospheric neutrinos and antineutrinos interacting with the rock surrounding the detector. These muons can then either stop in the detector, called "stopping muons," or pass through the detector, called "through-going muons." Typically the stopping muons have an $\mathcal{O}(10\ {\rm GeV})$ energy while the through-going muons have an $\mathcal{O}(100\ {\rm GeV})$ energy. Although statistically not as significant as the contained events, these data provide important information in this higher energy range.

Our analysis of these events exactly follows that given in Refs. [89,90]. We do not include the effects of the muon energy fluctuations as was recently done in Ref. [30]. The detection rate for stopping muons, S, and through-going muons, T, is given by

$$\frac{{\rm d}N^n_{\mu,S,T}}{{\rm d}t} = N_A \int_0^\infty {\rm d}E_\nu \int_{\theta^{n,\min}}^{\theta^{n,\max}} {\rm d}\cos\theta_\nu \int_0^{E_\nu} {\rm d}E_\mu \times \frac{{\rm d}^2\,\Phi_\alpha(E_\nu,\cos\theta_\nu)}{{\rm d}E_\nu\,{\rm d}\cos\theta_\nu}\,\tilde{\mathcal{P}}_{\alpha\mu}(E_\nu,\cos\theta_\nu) \times \frac{{\rm d}\sigma_\mu(E_\nu;\,E_\mu)}{{\rm d}E_\mu}\mathcal{R}(E_\mu,E_{th})\,A_{S,T}(E_{th},\cos\theta_\nu). \tag{A10}$$

We assume, appropriate for these high energies, that the scattering is forward. This allows us to replace the charged lepton angle ϑ with the neutrino angle θ_ν; we may also perform the integration over the scattering angles θ_s and ϕ_s in the cross section. N_A is Avogadro's number. The function $\mathcal{R}(E_\mu, E_{th})$ is the average distance that a muon of energy E_μ will travel until its energy reaches the value E_{th}, the amount of energy needed to traverse the detector; this quantity is expressed in the natural units for range, distance times Earth's density. $A_T(E_{th},\cos\theta_\nu)$ is the area projected onto a plane perpendicular to the muon direction such that a muon of energy E_{th} or greater can pass through this part of the detector. The details for calculating $A_T(E_{th},\cos\theta_\nu)$ can be found in Ref. [91]. For the stopping muons, $A_S(E_{th},\cos\theta_\nu) = A(\ell_{\min},\cos\theta_\nu) - A_T(E_{th},\cos\theta_\nu)$, where $A(\ell_{\min},\cos\theta_\nu)$ is the projected area of the detector with a path length greater than $\ell_{\min}$ taken to be 7 m by the experimentalists. Note that there are only muon data as electrons/positrons produced in the rock are unable to travel to the detector. The data cover the angular region from $\cos\theta_\nu = 0$ to $\cos\theta_\nu = -1$, directions where muon production from the rock exceeds the cosmic ray background. Since the neutrinos can originate as either electron or muon neutrinos, we sum over the two neutrino flavors α as in Eq. (A10). The upgoing muon data are binned in ten angular bins and not binned in energy, resulting in a total of 20 data points.

Analysis of these events is not as computationally intensive as the calculation of the contained events since the forward scattering allows the integration over the scattering angles and the muon energy E_μ to be performed outside the fitting program. The parameters being fit are contained in $\tilde{\mathcal{P}}_{\alpha\mu}(E_\nu,\cos\theta_\nu)$, which is independent of the muon energy and scattering angle. We find it efficient to change the integration over these variables to the Feynman scaling variables x and y, as is natural for the deeply inelastic region.

3. Super-K statistical analysis

We use the most recent experimental data from Ref. [16], which includes 180 data points for fully contained single-ring events, 90 for fully contained multiring events, 80 for partially contained events, ten for upward through-going muons, and ten for upward stopping muons; in all, this constitutes 370 data points. To determine the neutrino oscillation parameters, we construct a χ^2 based upon a Poisson distribution, following the same procedure used in Ref. [16]. We incorporate systematic errors by utilizing the "pull" approach as described in Ref. [92], which allows us to incorporate systematic errors in the analysis without adding adjustable parameters. The approach is based upon allowing linear corrections to the theoretical predictions for each systematic error. Our χ^2 function is

$$\chi^2 = \sum_{n=1}^{370}\left\{2[\overline{N}_{\rm the}(n) - N_{\rm obs}(n)] + 2N_{\rm obs}(n)\ln\left(\frac{N_{\rm obs}(n)}{\overline{N}_{\rm the}(n)}\right)\right\} + \sum_{i=1}^{43}\left(\frac{\xi_i}{\sigma_i}\right)^2. \tag{A11}$$

$N_{\rm obs}(n)$ is the number of observed events in the bin n; $N_{\rm the}(n)$ is the theoretical prediction of the number of events in that bin; ξ_i is the systematic error pull for the systematic error i; and σ_i is the one-σ value for the systematic error i. $\overline{N}_{\rm the}(n)$ represents a modified prediction of the expected number of events due to the inclusion of systematic errors; the systematic errors adjust this quantity through an assumed linear dependence on the pulls ξ_i. Here we use 45 systematic errors arising from different inputs into the data analysis as described in Tables 7 through 10 taken from Ref. [15]. For these 45 errors, all of them contributed to the χ^2 except the overall flux normalization and the normalization for the multi-GeV multiring sample, which are floated freely. During each fit, these 45 ξ_i are varied to minimize χ^2 for a given set of oscillation parameters. The minimization of χ^2 with respect to ξ_i ($\frac{\partial\chi^2}{\partial\xi_j} = 0$) is equivalent in the pull method to numerically solving for ξ_i in the 45

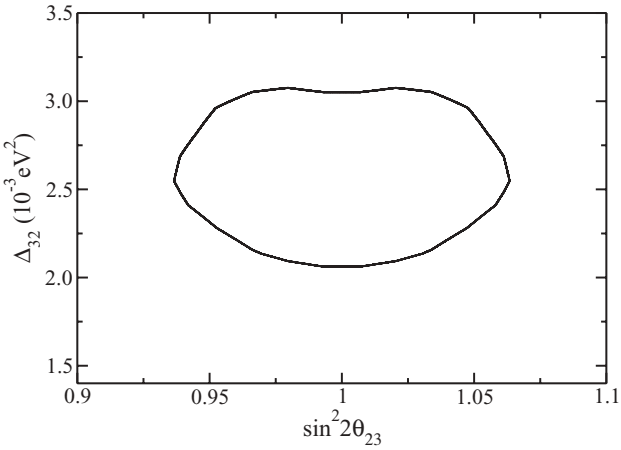

FIG. 7. Allowed region at $\Delta\chi^2 = 4.61$ for Δ_{32} and $\sin^2 2\theta_{23}$ in the subdominant approximation using only Super-K atmospheric data.

coupled equations of the form

$$\frac{\partial\chi^2}{\partial\xi_j} = \sum_{n=1}^{370} f_j^n \left(N_{th}(n) - \frac{N_{\rm obs}(n)}{1 + \sum_{i=1}^{45} f_i^n \cdot \xi_i} \right) + \sum_{i=1}^{43} \frac{\xi_i}{\sigma_i^2}\delta_{ij} = 0, \tag{A12}$$

where f_i^n is the ith systematic error for bin n. These equations are linearized and solved as a set of coupled linear equations.

We compare our analysis with that performed by the experimentalists in Ref. [16]. To do this, we utilize the subdominant approximation in Eq. (2) and minimize the above χ^2. Our best fit oscillation parameters are $(\Delta_{32}, \sin^2\theta_{23}, \theta_{13}) = (2.5 \times 10^{-3}\ \text{eV}^2, 0.51, 0.01)$ with an overall χ^2 of 416 for the 370 data points. In Fig. 1(a), the (black) solid curve represents $\Delta\chi^2$ versus Δ_{32} for the subdominant approximation, using only atmospheric data. In Fig. 7, we present the allowed region for Δ_{32} and $\sin^2 2\theta_{23}$ corresponding to $\Delta\chi^2 = 4.61$. We also present $\Delta\chi^2$ versus $\sin^2\theta_{23}$ in Fig. 8.

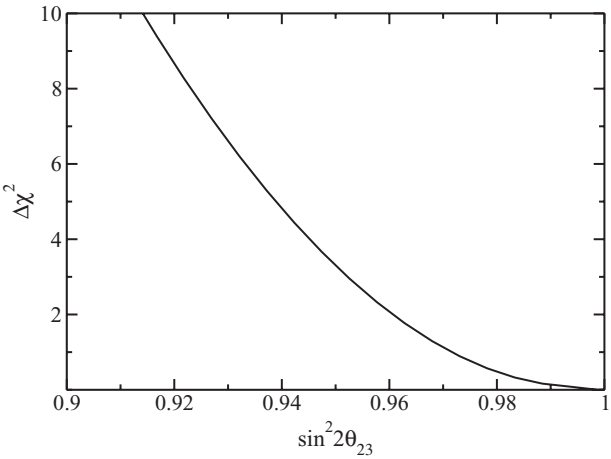

FIG. 8. $\Delta\chi^2$ versus $\sin^2 2\theta_{23}$ for our analysis of the recent Super-K atmospheric data in the subdominant approximation. Both Δ_{32} and θ_{13} are varied in obtaining this curve.

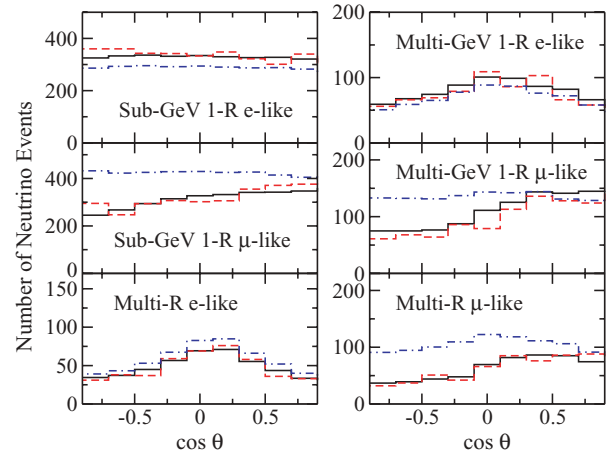

FIG. 9. (Color online) The top two graphs depict the number of events for the sub-GeV data as a function of the angular bin in $\cos\vartheta$, the middle two graphs are the same except for the multi-GeV data, and the bottom two graphs are for the multiring events. The (black) solid curves represent the results from our best fit parameters, the (red) dashed curves represent the data, and the (blue) dot-dashed curves represent the Monte Carlo no-oscillation predictions.

For $\Delta\chi^2 = 4.61$, we find the allowed parameter values $2.1 \times 10^{-3}\ \text{eV}^2 < \Delta_{32} < 3.1 \times 10^{-3}\ \text{eV}^2$ and $0.938 < \sin^2 2\theta_{23}$. Additionally, we extract the allowed value for θ_{13} from the (black) solid curve in Fig. 3(a), $-0.38 < \theta_{13} < 0.38$. This is exactly the result of Ref. [16] and our other results are in excellent agreement with that analysis. As noted previously, our reproduction of the allowed region for θ_{13}, which has a nonzero but small effect on the atmospheric data, is a very strong test of our analysis.

Finally, in Figs. 9 and 10, we compare the predicted number of neutrino events corresponding to our best fit parameters with the experimental data as a function of the zenith angle. We also present the Monte Carlo predictions for the expected number of events in the absence of neutrino oscillations. Each

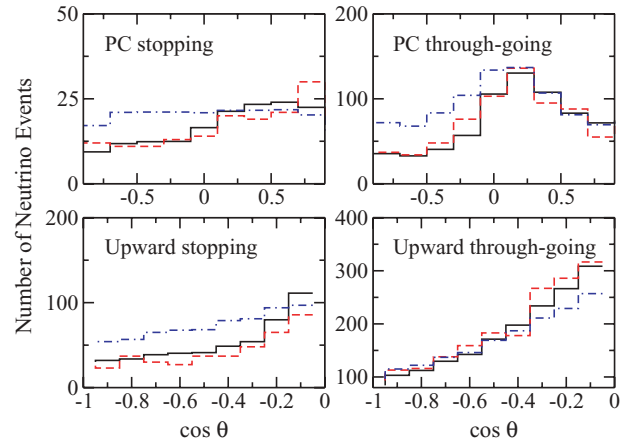

FIG. 10. (Color online) The same as Fig. 9 except the data sets are now the partially contained stopping events (upper left), the partially contained through-going events (upper right), the upward stopping muon events (lower left), and the upward through-going muon events (lower right).

of the different Super-K atmospheric data sets are depicted. The results are a good fit to the data, comparable to that found in Ref. [16].

4. CHOOZ experiment

For the CHOOZ reactor experiment, we follow a standard procedure as described in Ref. [21]. In our analysis, we use experimental data that consist of seven positron energy bins for each of the two reactors, giving a total of 14 bins. We include a 14×14 covariance matrix, V_{ij}^{-1}, to account for the correlation between the energy bins, and we include the systematic error from the overall normalization and energy calibration. We write the expected positron yield for the kth reactor and the jth energy spectrum bin as

$$\overline{X}(E_j, L_k, \theta, \Delta_{32}) = \tilde{X}(E_j)\overline{P}(E_j, L_k, \theta, \Delta_{32}), \quad (j = 1, \ldots, 7, k = 1, 2), \tag{A13}$$

where $\tilde{X}(E_j)$ is the distance-independent positron yield in the absence of neutrino oscillations, L_k is the reactor-detector distance, and $\overline{P}(E_j, L_k, \theta, \Delta_{32})$ is the oscillation probability averaged over the energy bin and the detector and reactor core sizes. In our fitting routine, we minimize the following χ^2 function with respect to the neutrino oscillation parameters

$$\chi^2(\theta, \Delta_{32}, \alpha, g) = \sum_{i=1}^{14}\sum_{j=1}^{14}[X_i - \alpha\overline{X}(gE_i, L_i, \theta, \Delta_{32})] \times V_{ij}^{-1}[X_j - \alpha\overline{X}(gE_j, L_j, \theta, \Delta_{32})] + \left(\frac{\alpha - 1}{\sigma_\alpha}\right)^2 + \left(\frac{g-1}{\sigma_g}\right)^2, \tag{A14}$$

with the absolute normalization constant α and the energy-scale calibration factor g.

5. K2K experiment

For the K2K experiment [17,18], we employ the method developed in Ref. [18] to estimate the expected no-oscillation neutrino spectrum, $S(E_\nu)$, in the relevant energy range of $\sim$0.2 to $\sim$3.0 GeV. The expected number of neutrino events for oscillating neutrinos is then

$$N_n^{\text{theo}} = \int_{E_{\min}(n)}^{E_{\max}(n)} S(E_\nu) P_{\mu\mu}(L/E_\nu), \tag{A15}$$

where $P_{\mu\mu}(L/E_\nu)$ is the muon neutrino survival probability and $E_{\max}(n)$ ($E_{\min}(n)$) are the maximum (minimum) energy values for the energy bin n. For the statistical analysis, we follow the procedure described in Ref. [93]. We only use the single-ring subsample, which consists of 58 neutrino events. The signature for neutrino oscillations from ν_μ to ν_τ in a two-neutrino analysis are both a reduction in the total number of observed neutrino events and a distortion in the neutrino energy spectrum. The χ^2 function is divided into two terms: the observed total number of events detected at the Super-K detector, χ^2_{norm}, and the shape of the spectrum included in χ^2_{shape}. We use the "pull" method [92] to account for 31 systematic uncertainties by adding a third term χ^2_{syst}:

$$\chi^2_{\text{K2K}} = \chi^2_{\text{norm}} + \chi^2_{\text{shape}} + \chi^2_{\text{syst}}. \tag{A16}$$

The best fit oscillation parameters, Δ_{32} and θ_{23}, are obtained by minimizing χ^2_{K2K}.

The systematic parameters included in χ^2_{syst} arise from the neutrino energy spectrum at the near detector site, the flux ratio, the neutrino-nucleus cross section, the efficiency and the energy scale of the Super-K detector, and the overall normalization. The kth systematic error is represented by the coefficient C_n^k and modifies the expected number of neutrino events, Eq. (A15), in a linear manner according to the "pull" method

$$\tilde{N}_n^{\text{theo}} = N^{\text{theo}}(n) + \sum_{k=1}^{31} C_n^k \xi_k, \qquad \tilde{N}_{\text{total}}^{\text{theo}} = \sum_{n=1}^{8} \tilde{N}_n^{\text{theo}}, \tag{A17}$$

with ξ_k the pull corresponding to systematic error k.

Due to the low statistics, we employ a Poisson distribution; hence, the expressions for χ^2_{norm} and χ^2_{shape} are given by

$$\chi^2_{\text{norm}} = 2\left(\tilde{N}_{\text{total}}^{\text{theo}} - N_{\text{total}}^{\text{data}} - N_{\text{total}}^{\text{data}} \ln \frac{\tilde{N}_{\text{total}}^{\text{theo}}}{N_{\text{total}}^{\text{data}}}\right), \qquad \chi^2_{\text{shape}} = 2\sum_{n=1}^{8}\left(\tilde{N}_n^{\text{theo}} - N_n^{\text{data}} - N_n^{\text{data}} \ln \frac{\tilde{N}_n^{\text{theo}}}{N_n^{\text{data}}}\right), \tag{A18}$$

where N_n^{data} is the experimental data provided by the K2K collaboration [18] and the superscript "total" implies a sum over n. The contribution to χ^2 from the systematic errors is

$$\chi^2_{\text{syst}} = \sum_{j,k=1}^{31} \xi_k M_{kj}^{-1} \xi_j, \tag{A19}$$

where we use an error matrix M_{kj} constructed from Tables 8.1 and 8.2 provided in Ref. [93].

In Fig. 11, we depict $\Delta\chi^2$ versus Δ_{32} for an analysis that utilizes only the K2K data in the subdominant approximation;

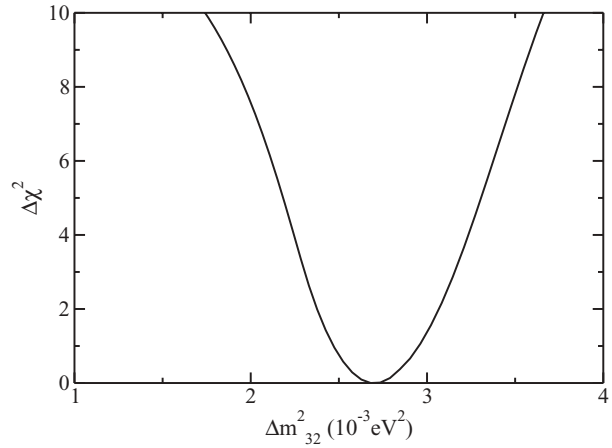

FIG. 11. $\Delta\chi^2$ versus Δ_{32} for our analysis of the K2K experiment in the subdominant approximation.

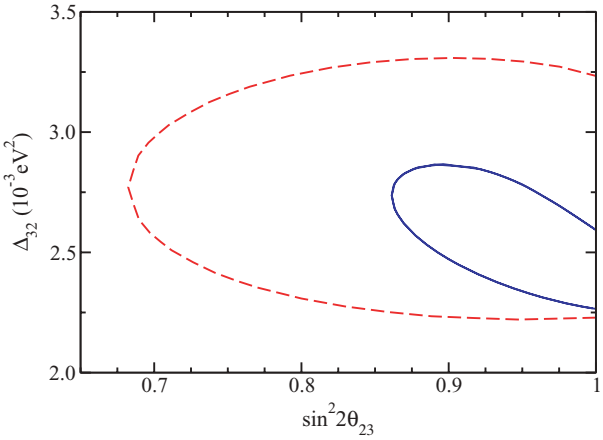

FIG. 12. (Color online) Δ_{32} versus $\sin^2 2\theta_{23}$ allowed region at $\Delta\chi^2 = 4.61$ for a two parameter fit in the subdominant approximation for the K2K, (red) dashed line, and the MINOS, (blue) solid line, experiments.

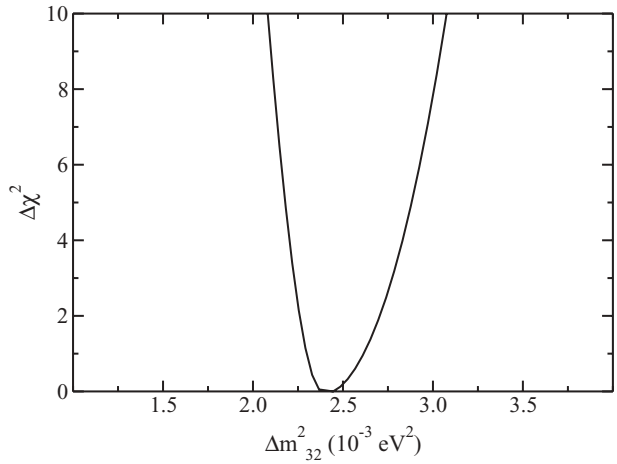

FIG. 13. The same as Fig. 11 except the data are from MINOS.

also, Fig. 12 shows the allowed region corresponding to $\Delta\chi^2 = 4.61$ in the (red) dashed contour for Δ_{32} and $\sin^2 2\theta_{23}$ in the subdominant approximation. The absolute minimum in our fit is $(\Delta_{32}, \sin^2 2\theta_{23}) = (2.78 \times 10^{-3}\ \text{eV}^2, 0.998)$. We find $2.2 \times 10^{-3}\ \text{eV}^2 < \Delta_{32} < 3.2 \times 10^{-3}\ \text{eV}^2$. The total number of observed events, 58, is in agreement with the 56 events found from the model. All of these results are consistent with the analysis performed by the experimentalists in Ref. [18].

6. MINOS experiment

The MINOS experiment is quite similar to the K2K experiment and thus we apply a similar analysis technique. For the no-oscillation spectrum, we use the Monte Carlo simulation provided by the MINOS collaboration [20]. We normalized this spectrum to measurements made at the near detector. A total of 1065 events were expected in the absence of neutrino oscillations. With the no-oscillation spectrum and Eq. (A15), we calculate the expected number of neutrino events in the presence of neutrino oscillations. We use the MINOS data [20] corresponding to two years of beam operation in which 884 ν_μ neutrino events are observed. The data consist of 15 energy bins along with three systematic errors: the relative normalization between the far and near detectors with a 4% uncertainty; the absolute hadronic energy scale with a 11% uncertainty; and a 50% uncertainty in the neutral-current background rate. For the definition of χ^2, we use the Poisson distribution function

$$\chi^2_{\text{MINOS}} = 2\sum_{n=1}^{15}\left(\tilde{N}_n^{\text{theo}} - N_n^{\text{data}} - N_n^{\text{data}} \ln\frac{\tilde{N}_n^{\text{theo}}}{N_n^{\text{data}}}\right) + \sum_{j=1}^{3}\left(\frac{\xi_j}{\sigma_j}\right)^2, \tag{A20}$$

where the symbols are analogously defined to those in the K2K section.

In Fig. 13 we plot $\Delta\chi^2$ versus Δ_{32} for the K2K data in the subdominant approximation; likewise, in Fig. 12, we present the allowed region corresponding to $\Delta\chi^2 = 4.61$, the blue solid curve, for Δ_{32} and $\sin^2 2\theta_{23}$. The minimum of χ^2 is located at $\Delta_{32} = 2.41 \times 10^{-3}\ \text{eV}^2$ and $\sin^2 2\theta_{23} = 0.9990$. The allowed intervals of these parameters are $2.25 \times 10^{-3}\ \text{eV}^2 < \Delta_{32} < 2.8 \times 10^{-3}\ \text{eV}^2$ and $0.86 < \sin^2 2\theta_{23}$. All of these results are consistent with the analysis performed by the experimentalists in Ref. [20].

Results that combine CHOOZ, K2K, and MINOS are presented in the main body of this work. This appendix provides details of the analysis tools we use throughout this work; additional details may be found in Ref. [79].

[1] Y. Fukuda *et al.* (Kamiokande Collaboration), Phys. Rev. Lett. **77**, 1683 (1996).
[2] M. B. Smy *et al.* (Super-Kamiokande Collaboration), Phys. Rev. D **69**, 011104(R) (2004).
[3] B. T. Cleveland *et al.*, Astrophys. J. **496**, 505 (1998).
[4] W. Hampel *et al.* (GALLEX Collaboration), Phys. Lett. **B447**, 127 (1999).
[5] J. N. Abdurashitov *et al.* (SAGE Collaboration), J. Exp. Theor. Phys. **95**, 181 (2002).
[6] M. Altmann *et al.* (GNO Collaboration), Phys. Lett. **B616**, 174 (2005).
[7] S. N. Ahmed *et al.* (SNO Collaboration), Phys. Rev. Lett. **92**, 181301 (2004).
[8] B. Aharmim *et al.* (SNO Collaboration), Phys. Rev. C **72**, 055502 (2005).
[9] B. Aharmim *et al.* (SNO Collaboration), Phys. Rev. C **75**, 045502 (2007).
[10] B. Aharmim *et al.* (SNO Collaboration), Phys. Rev. Lett. **101**, 111301 (2008).

[11] T. Araki *et al.* (KamLAND Collaboration), Phys. Rev. Lett. **94**, 081801 (2005).
[12] S. Abe *et al.* (KamLAND Collaboration), Phys. Rev. Lett. **100**, 221803 (2008).
[13] Y. Fukuda *et al.* (Super-Kamiokande Collaboration), Phys. Rev. Lett. **81**, 1562 (1998).
[14] S. Fukuda *et al.* (Super-Kamiokande Collaboration), Phys. Rev. Lett. **85**, 3999 (2000).
[15] Y. Ashie *et al.* (Super-Kamiokande Collaboration), Phys. Rev. Lett. **93**, 101801 (2004).
[16] J. Hosaka *et al.* (Super-Kamiokande Collaboration), Phys. Rev. D **74**, 032002 (2006).
[17] E. Aliu *et al.* (K2K Collaboration), Phys. Rev. Lett. **94**, 081802 (2005).
[18] M. H. Ahn *et al.* (K2K Collaboration), Phys. Rev. D **74**, 072003 (2006).
[19] P. Adamson *et al.* (MINOS Collaboration), Phys. Rev. D **77**, 072002 (2008).
[20] P. Adamson *et al.* (MINOS Collaboration), Phys. Rev. Lett. **101**, 131802 (2008).
[21] M. Apollonio *et al.* (CHOOZ Collaboration), Phys. Lett. **B466**, 415 (1999).
[22] M. Gronau, R. Johnson, and J. Schechter, Phys. Rev. D **32**, 3062 (1985).
[23] H. Harari and M. Leurer, Phys. Lett. **B181**, 123 (1986).
[24] T. Schwetz, M. A. Tortola, and J. W. F. Valle, New J. Phys. **10**, 113011 (2008).
[25] A. B. Balantekin and D. Yilmaz, J. Phys. G **35**, 075007 (2008).
[26] G. L. Fogli, E. Lisi, A. Marrone, A. Palazzo, and A. M. Rotunno, Phys. Rev. Lett. **101**, 141801 (2008).
[27] G. L. Fogli, E. Lisi, A. Marrone, A. Palazzo, and A. M. Rotunno (2009), arXiv:0905.3549 [hep-ph].
[28] M. Maltoni and T. Schwetz (2008), arXiv:0812.3161 [hep-ph].
[29] J. E. Roa, D. C. Latimer, and D. J. Ernst, Phys. Rev. Lett. **103**, 061804 (2009).
[30] M. C. Gonzalez-Garcia and M. Maltoni, Phys. Rep. **460**, 1 (2008).
[31] G. L. Fogli, E. Lisi, A. Marrone, and A. Palazzo, Prog. Part. Nucl. Phys. **57**, 742 (2006).
[32] X. Guo *et al.* (Daya Bay Collaboration) (2007), arXiv:hep-ex/0701029.
[33] F. Ardellier *et al.* (Double CHOOZ Collaboration) (2006), arXiv:hep-ex/0606025.
[34] K. K. Joo (RENO Collaboration), Nucl. Phys. Proc. Suppl. **168**, 125 (2007).
[35] Y. Oyama (2005), arXiv:hep-ex/0512041.
[36] P. F. Harrison, D. H. Perkins, and W. G. Scott, Phys. Lett. **B530**, 167 (2002).
[37] S. F. King (2009), arXiv:0903.3199 [hep-ph]; (2009), arXiv:0904.3255 [hep-ph].
[38] L. Wolfenstein, Phys. Rev. D **18**, 958 (1978).
[39] P. F. Harrison and W. G. Scott, Phys. Lett. **B535**, 163 (2002).
[40] J. D. Bjorken, P. F. Harrison, and W. G. Scott, Phys. Rev. D **74**, 073012 (2006).
[41] X.-G. He and A. Zee, Phys. Lett. **B645**, 427 (2007).
[42] G. Altarelli and F. Feruglio, Nucl. Phys. **B720**, 64 (2005).
[43] E. Ma and G. Rajasekaran, Phys. Rev. D **64**, 117303 (2001).
[44] O. L. G. Peres and A. Y. Smirnov, Nucl. Phys. Proc. Suppl. **110**, 355 (2002).
[45] O. L. G. Peres and A. Y. Smirnov, Nucl. Phys. **B680**, 479 (2004).
[46] D. C. Latimer and D. J. Ernst, Phys. Rev. D **71**, 017301 (2005).
[47] D. C. Latimer and D. J. Ernst, Phys. Rev. C **71**, 062501(R) (2005).
[48] D. C. Latimer and D. J. Ernst, Phys. Rev. C **72**, 045502 (2005).
[49] D. C. Latimer, J. Escamilla, and D. J. Ernst, Phys. Rev. C **76**, 055502 (2007).
[50] S. Palomares-Ruiz and J. Bernabeu, Nucl. Phys. Proc. Suppl. **138**, 398 (2005).
[51] S. Palomares-Ruiz and S. T. Petcov, Nucl. Phys. **B712**, 392 (2005).
[52] D. Indumathi and M. V. N. Murthy, Phys. Rev. D **71**, 013001 (2005).
[53] S. T. Petcov and T. Schwetz, Nucl. Phys. **B740**, 1 (2006).
[54] R. Gandhi, P. Ghoshal, S. Goswami, P. Mehta, S. U. Sankar, and S. Shalgar, Phys. Rev. D **76**, 073012 (2007).
[55] R. Gandhi, P. Ghoshal, S. Goswami, and S. U. Sankar (2008), arXiv:0805.3474 [hep-ph].
[56] A. Samanta, Phys. Rev. D **79**, 053011 (2009); (2009), arXiv:0907.3540 [hep-ph]; Phys. Rev. D **80**, 073008 (2009).
[57] R. Gandhi, P. Ghoshal, S. Goswami, and S. U. Sankar (2009), arXiv:0905.2382 [hep-ph].
[58] T. Ohlsson and H. Snellman, J. Math. Phys. **41**, 2768 (2000).
[59] T. Ohlsson and H. Snellman, Phys. Lett. **B474**, 153 (2000).
[60] S. P. Mikheev and A. Y. Smirnov, Sov. J. Nucl. Phys. **42**, 913 (1985).
[61] L. Wolfenstein, Phys. Rev. D **17**, 2369 (1978).
[62] A. M. Dziewonski and D. L. Anderson, Phys. Earth Planet. Inter. **25**, 297 (1981).
[63] V. K. Ermilova, V. A. Tsarev, and V. A. Chechin, Kratk. Soobshch. Fiz. **5**, 26 (1986).
[64] Q. Y. Liu, S. P. Mikheyev, and A. Y. Smirnov, Phys. Lett. **B440**, 319 (1988).
[65] E. K. Akhmedov, Sov. J. Nucl. Phys. **47**, 301 (1988).
[66] E. K. Akhmedov, A. Dighe, P. Lipari, and A. Y. Smirnov, Nucl. Phys. **B542**, 3 (1999).
[67] S. T. Petcov, Phys. Lett. **B434**, 321 (1998).
[68] E. K. Akhmedov, Nucl. Phys. **B538**, 25 (1999).
[69] M. V. Chizhov and S. T. Petcov, Phys. Rev. D **63**, 073003 (2001).
[70] E. K. Akhmedov, M. Maltoni, and A. Y. Smirnov, Phys. Rev. Lett. **95**, 211801 (2005).
[71] E. K. Akhmedov, M. Maltoni, and A. Y. Smirnov, J. High Energy Phys. 05 (2007) 077.
[72] E. K. Akhmedov, M. Maltoni, and A. Y. Smirnov, J. High Energy Phys. 06 (2008) 072.
[73] M. Koike, T. Ota, M. Saito, and J. Sato, Phys. Lett. **B675**, 69 (2009).
[74] E. K. Akhmedov, R. Johansson, M. Lindner, T. Ohlsson, and T. Schwetz, J. High Energy Phys. 04 (2004) 078.
[75] S. Choubey and P. Roy, Phys. Rev. D **73**, 013006 (2006).
[76] A. Takamura and K. Kimura, J. High Energy Phys. 01 (2006) 053.
[77] O. L. G. Peres and A. Y. Smirnov, Phys. Rev. D **79**, 113002 (2009).
[78] D. V. Ahluwalia, Mod. Phys. Lett. A **13**, 2249 (1998).
[79] J. E. Roa, Ph.D. thesis, Vanderbilt University (December 2008).
[80] J. Escamilla, D. C. Latimer, and D. J. Ernst, AIP Conf. Proc. **947**, 227 (2007).
[81] J. Escamilla, D. J. Ernst, and D. C. Latimer, AIP Conf. Proc. **991**, 153 (2008).
[82] M. Honda, T. Kajita, K. Kasahara, and S. Midorikawa, Phys. Rev. D **70**, 043008 (2004).
[83] T. K. Gaisser and T. Stanev, Phys. Rev. D **57**, 1977 (1998).

[84] M. C. Gonzalez-Garcia and Y. Nir, Rev. Mod. Phys. **75**, 345 (2003).
[85] K. C. Hannabuss and D. C. Latimer, J. Phys. A **33**, 1369 (2000).
[86] B. D. Keister and W. N. Polyzou (2009), arXiv:0908.1404 [hep-ph].
[87] M. D. Messier, Ph.D. thesis, Boston University (1999).
[88] M. Ishitsuka, Ph.D. thesis, University of Tokyo (2004).
[89] N. Fornengo, M. C. Gonzalez-Garcia, and J. W. F. Valle, J. High Energy Phys. 07 (2000) 006.
[90] M. C. Gonzalez-Garcia, M. Maltoni, C. Pena-Garay, and J. W. F. Valle, Phys. Rev. D **63**, 033005 (2001).
[91] P. Lipari and M. Lusignoli, Phys. Rev. D **58**, 073005 (1998).
[92] G. L. Fogli, E. Lisi, A. Marrone, D. Montanino, and A. Palazzo, Phys. Rev. D **66**, 053010 (2002).
[93] M. Hasegawa, Ph.D. thesis, Kyoto University (January 2006).